

Electronic Supplementary Information for:
The chiral magnetic nanomotors

Konstantin I. Morozov* and Alexander M. Leshansky

Department of Chemical Engineering,

Technion – Israel Institute of Technology, Haifa 32000, Israel

(Dated: November 6, 2013)

* mrk@tx.technion.ac.il

I. Effectiveness of the rotating magnetic field vs. the gradient field for particle propulsion

The particle with the magnetic moment \mathcal{M} can be involved into translational motion by the gradient magnetic field ∇H . The velocity acquired by the particle in this field is $U_{grad} \sim \mathcal{M}\nabla H/\xi$. Here ξ is the translational viscous resistance coefficient with the characteristic value $\xi \sim 2\pi\eta L$, where η is the dynamic viscosity, and L is the characteristic size of the particle.

The translational motion can be initiated by the rotating magnetic field of amplitude H if the particle possesses chirality. The velocity acquired by the particle in rotating field $U_{rot} \sim \Omega R \text{Ch}$, where Ω is the angular velocity of the particle rotation and R is the rotation radius. The chirality coefficient Ch is determined by the geometry of the particle, its typical values for helices are $\text{Ch} \sim 0.1 \div 0.3$ (see Fig. 5 in the main text). The characteristic value of the angular velocity Ω is found from the balance of the external magnetic torque and viscous torque $\Omega \sim \mathcal{M}H/\kappa$, where κ is the rotational drag coefficient. For a slender particle rotating around its longer axis $\kappa \sim 4\pi\eta R^2 L$. The ratio of both velocities is

$$\frac{U_{rot}}{U_{grad}} \sim \text{Ch} \frac{H}{R\nabla H}. \quad (\text{S1})$$

Let us estimate this ratio for particles with the characteristic size $R \sim 1 \mu\text{m}$. The maximal value of the magnetic field gradients achieved in modern MRI devices is $\nabla H \sim 10^3 \text{ Oe/cm}$. Substituting this value into Eq. (S1) and using the above estimate for Ch we find that the ratio $U_{rot}/U_{grad} \sim 1$ already at very low amplitudes $H \sim 1 \text{ Oe}$ of the rotating magnetic field. In other words, the rotating magnetic field with the amplitude comparable to the magnetic field of the Earth, propels the particle with the same velocity as the extremal gradient magnetic field does. Thus, comparing standard experimental set-up with amplitudes of the rotating field $H \sim 10 \div 10^2 \text{ Oe}$ and the field gradients $\nabla H \sim 1 \text{ Oe/cm}$, the rotating field yields a propulsion speed of four to five orders of magnitude higher than that due to the gradient magnetic field.

II. Rotation matrix

We use the definition of the three Euler angles φ , θ and ψ following Ref. [2]. The components of any vector \mathbf{W} in the body-fixed coordinate system (BCS) and in the laboratory

coordinate system (LCS) are determined from the relation $\mathbf{W}^{BCS} = \mathbf{R} \cdot \mathbf{W}$, where \mathbf{R} is the rotation matrix. The rotation matrix is expressed explicitly via the Euler angles [3]

$$\mathbf{R} = \begin{pmatrix} c_\varphi c_\psi - s_\varphi s_\psi c_\theta & s_\varphi c_\psi + c_\varphi s_\psi c_\theta & s_\psi s_\theta \\ -c_\varphi s_\psi - s_\varphi c_\psi c_\theta & -s_\varphi s_\psi + c_\varphi c_\psi c_\theta & c_\psi s_\theta \\ s_\varphi s_\theta & -c_\varphi s_\theta & c_\theta \end{pmatrix},$$

where we use the compact notation, $s_\psi = \sin \psi$, $c_\theta = \cos \theta$, etc.

III. Stability of the low-frequency solution

In this section we study the stability of the low-frequency synchronous stationary solution. It is characterized by the following values of the Euler angles: $\psi = 0$, $\theta = \pi/2$. The third angle $\tilde{\varphi} \equiv \varphi - \omega t$ reads

$$\tilde{\varphi} = \varphi_0 - \arcsin(\omega/\omega_c^{(I)}), \quad (\text{S2})$$

where $\omega_c^{(I)} = \sqrt{A^2 + B^2}$ and φ_0 is the angle between the total magnetic moment \mathbf{M} of the particle and its transverse component \mathbf{m} .

To study the stability of this stationary solution we perturb it by adding small disturbances $\psi'(t)$, $\theta'(t)$ and $\tilde{\varphi}'(t)$:

$$\psi \rightarrow 0 + \psi'(t), \quad \theta \rightarrow \pi/2 + \theta'(t), \quad \tilde{\varphi} \rightarrow \tilde{\varphi} + \tilde{\varphi}'(t). \quad (\text{S3})$$

Substitution of these relations into the equations of motion (see Eqs. (6)-(8) in the main text) and linearization over the small perturbations leads to the following system of equations

$$\dot{\tilde{\varphi}}'(t) = -[As_{\tilde{\varphi}} + Bc_{\tilde{\varphi}}]\tilde{\varphi}'(t), \quad (\text{S4})$$

$$\dot{\theta}'(t) = -As_{\tilde{\varphi}}\theta'(t) + Bs_{\tilde{\varphi}}\psi'(t), \quad (\text{S5})$$

$$\dot{\psi}'(t) = [\omega + Cs_{\tilde{\varphi}}]\theta'(t) - Cc_{\tilde{\varphi}}\psi'(t). \quad (\text{S6})$$

The perturbation $\tilde{\varphi}'(t)$ appears to be decoupled from the other two perturbations. Using the stationary solution (S2) the Eq. S4 reduces to

$$\dot{\tilde{\varphi}}'(t) = -\sqrt{\omega_c^{(I)2} - \omega^2} \tilde{\varphi}'(t). \quad (\text{S7})$$

It describes the decay of the perturbation $\tilde{\varphi}'(t)$ in the whole interval $[0, \omega_c^{(I)}]$ of existence of the low-frequency synchronous solution.

To study the dynamics of coupled perturbations $\psi'(t)$ and $\theta'(t)$ we write them in the form $\sim e^{\lambda t}$. In this way we obtain the homogenous system of algebraic equations for the perturbation amplitudes ψ and θ

$$(\lambda + As_{\tilde{\varphi}})\theta - Bs_{\tilde{\varphi}}\psi = 0, \quad (\text{S8})$$

$$-(\omega + Cs_{\tilde{\varphi}})\theta + (\lambda + Cs_{\tilde{\varphi}})\psi = 0. \quad (\text{S9})$$

The increment λ is found from the condition of equality to zero of the determinant of the system:

$$\lambda^2 + \lambda(As_{\tilde{\varphi}} + Cs_{\tilde{\varphi}}) + s_{\tilde{\varphi}}(ACc_{\tilde{\varphi}} - BCs_{\tilde{\varphi}} - B\omega) = 0. \quad (\text{S10})$$

Using Eq. (S2), $Ac_{\tilde{\varphi}} - Bs_{\tilde{\varphi}} = \omega$, and then Eq. (S10) reduces to

$$\lambda^2 + \lambda(As_{\tilde{\varphi}} + Cs_{\tilde{\varphi}}) + s_{\tilde{\varphi}}\omega(C - B) = 0. \quad (\text{S11})$$

For a slender particle $\kappa_3 < \kappa_1$ and thus $C = mH/\kappa_3 > B = mH/\kappa_1$. Therefore, the development of the perturbations determines solely by the value of the coefficient $s_{\tilde{\varphi}}$. When $s_{\tilde{\varphi}} > 0$, both roots of Eq. (S11) are negative (or their real parts are negative) and the perturbations decay. For $s_{\tilde{\varphi}} < 0$, there appears a root with positive real part. It describes growth of perturbations: the low-frequency solution becomes unstable and it bifurcates into the high-frequency synchronous regime. The critical value for the transition is determined by the condition $s_{\tilde{\varphi}} = 0$. Taking into account Eq. (S2) and the definition of the angle φ_0 , i.e., $s_{\varphi_0} = A/\omega_c^{(I)}$, we finally find the critical value of the field frequency, $\omega_c = A$, delimiting the intervals of stability of the low-frequency ($\omega < A$) and high-frequency ($\omega > A$) synchronous solution.

IV. Rotational viscous resistance coefficients of a helix

We approximate the rotational viscous resistance coefficients of a helix by the corresponding values for a spheroid enclosing the helix. Let a and b be, correspondingly, the longitudinal (along the symmetry axis) and transversal semi-axes of spheroid. The respective resistances due to rotation around the symmetry axis and in perpendicular direction read [4]

$$\kappa_{\parallel} = 2\eta V n_{\perp}^{-1}, \quad \kappa_{\perp} = 2\eta V \frac{a^2 + b^2}{a^2 n_{\parallel} + b^2 n_{\perp}}, \quad (\text{S12})$$

where η is the dynamic viscosity of the liquid, V is the spheroid volume, n_{\parallel} and $n_{\perp} = (1 - n_{\parallel})/2$ are the depolarizing factors of the spheroid. For the prolate spheroid with $a > b$ and eccentricity $e = \sqrt{1 - b^2/a^2}$ the depolarizing factor along the symmetry axis reads [5]

$$n_{\parallel} = \frac{1 - e^2}{e^3} \left(\frac{1}{2} \ln \frac{1 + e}{1 - e} - e \right). \quad (\text{S13})$$

For the helical nanomotor with the aspect ratio $a/b = 4.5$ used in experiments [6], the following estimate is obtained using Eqs. (S12) and (S13)

$$\kappa_1/\kappa_3 = \kappa_{\perp}/\kappa_{\parallel} = 5.61. \quad (\text{S14})$$

V. Normal and binormal helices

In this section we provide a short description of geometrical properties of helices with non-circular cross-section. The more detailed information can be found in Ref. [7].

In the body-fixed coordinate system $x_1x_2x_3$ with the helix axis x_3 the coordinates of the helix centerline is

$$\mathbf{X}(s) = \left[R \cos(\lambda s), R \sin(\lambda s), \frac{P}{2\pi} \lambda s \right]. \quad (\text{S15})$$

Here R and P are the radius and the pitch of the helical filament, respectively; s is the arc length, and

$$\lambda = \frac{1}{\sqrt{R^2 + \frac{P^2}{4\pi^2}}}. \quad (\text{S16})$$

The variables R , P and λ can be expressed via curvature κ and torsion τ

$$\kappa = R\lambda^2, \quad \tau = \frac{P}{2\pi}\lambda^2. \quad (\text{S17})$$

The helix angle Θ is determined according to the relation

$$\tan \Theta = \kappa/\tau = 2\pi R/P. \quad (\text{S18})$$

We mention also the following simple relations for the helix angle Θ :

$$\sin \Theta = \kappa/\lambda = R\lambda, \quad \cos \Theta = \tau/\lambda = \frac{P}{2\pi}\lambda. \quad (\text{S19})$$

In terms of κ and τ Eq. (S15) can be written as

$$\mathbf{X}(s) = \left[\frac{\kappa}{\lambda^2} \cos(\lambda s), \frac{\kappa}{\lambda^2} \sin(\lambda s), \frac{\tau}{\lambda} s \right]. \quad (\text{S20})$$

Let $\{\mathbf{d}_1, \mathbf{d}_2, \mathbf{d}_3\}$ be a right-handed director basis defined at each point s along the axis of the filament. $\mathbf{d}_3 = \partial \mathbf{X}(s)/\partial s$ is the vector tangent to the centreline of the filament. Vectors \mathbf{d}_1 and \mathbf{d}_2 lie in the cross-sectional plane of the filament. The cross-section is assumed to be elliptic and the vector \mathbf{d}_2 is oriented with the longer axis of the cross-section.

There are two characteristic types of helices. For the *normal* helix, vector \mathbf{d}_1 aligned with the shorter cross-sectional axis has a constant (fixed) component along the x_3 -axis of helix. The local basis of the normal helix reads:

$$\begin{aligned}\mathbf{d}_1 &= \left[\frac{\tau}{\lambda} \sin(\lambda s), -\frac{\tau}{\lambda} \cos(\lambda s), \frac{\kappa}{\lambda} \right] . \\ \mathbf{d}_2 &= [\cos(\lambda s), \sin(\lambda s), 0] . \\ \mathbf{d}_3 &= \left[-\frac{\kappa}{\lambda} \sin(\lambda s), \frac{\kappa}{\lambda} \cos(\lambda s), \frac{\tau}{\lambda} \right] .\end{aligned}\tag{S21}$$

In the case of the *binormal* helix, vector \mathbf{d}_2 of the longer cross-section has a fixed component along the x_3 -axis of helix. The local basis of the binormal helix reads:

$$\begin{aligned}\mathbf{d}_1 &= [-\cos(\lambda s), -\sin(\lambda s), 0] . \\ \mathbf{d}_2 &= \left[\frac{\tau}{\lambda} \sin(\lambda s), -\frac{\tau}{\lambda} \cos(\lambda s), \frac{\kappa}{\lambda} \right] . \\ \mathbf{d}_3 &= \left[-\frac{\kappa}{\lambda} \sin(\lambda s), \frac{\kappa}{\lambda} \cos(\lambda s), \frac{\tau}{\lambda} \right] .\end{aligned}\tag{S22}$$

VI. Propulsion velocity of a rotating helix

Let us consider propulsion velocity $U \equiv U_3$ of a single rigid helix rotating about its helical axis (x_3) with a constant angular speed $\Omega \equiv \Omega_3$. The centerline of the helix *at rest* is given by Eq. (S15) above. For translating and rotating helix,

$$\mathbf{X}(s, t) = \left[R \cos(\lambda s + \Omega t), R \sin(\lambda s + \Omega t), \frac{P}{2\pi} \lambda s + U t \right] ,\tag{S23}$$

where U is yet undetermined propulsion velocity. The basic assumption of the local Resistive Force Theory (e.g. [1]) is that the local force per unit length (force density) exerted on the slender filament is given by

$$\mathbf{f} = f_{\perp}[\mathbf{u} - (\mathbf{u} \cdot \mathbf{d}_3) \mathbf{d}_3] + f_{\parallel}(\mathbf{u} \cdot \mathbf{d}_3) \mathbf{d}_3 ,\tag{S24}$$

where $\mathbf{d}_3 = \partial \mathbf{X}(s, t) / \partial s$ is the local tangent, $\mathbf{u} = \partial \mathbf{X}(s, t) / \partial t$ is the local velocity and f_\perp and f_\parallel are the drag coefficients corresponding to transverse and longitudinal motions.

We substitute the local velocity as $\mathbf{u} = \mathbf{u}_\perp + U \mathbf{e}_3$ (\mathbf{e}_3 is unit vector along x_3 -axis) into (S24) and setting the total force in the x_3 -direction to zero, we find that

$$U \int_0^L [f_\perp + (f_\parallel - f_\perp)(\mathbf{d}_3 \cdot \mathbf{e}_3)^2] ds = -(f_\parallel - f_\perp) \int_0^L (\mathbf{d}_3 \cdot \mathbf{u}_\perp)(\mathbf{d}_3 \cdot \mathbf{e}_3) ds. \quad (\text{S25})$$

Here L is the length of the helical filament. Substituting $\chi = f_\perp / f_\parallel$ and the expressions for the local tangent \mathbf{d}_3 and \mathbf{u}_\perp into (S25) one can derive the scaled propulsion velocity as a function of χ :

$$\frac{U}{\Omega R} = -\frac{B_\parallel}{\xi_\parallel R} = \frac{(\chi - 1) \sin 2\Theta}{2 [1 + (\chi - 1) \sin^2 \Theta]}. \quad (\text{S26})$$

For *exponentially thin* filament, $f_\perp = 2f_\parallel = 4\pi\eta E$, with a small parameter $E = 2/\ln \epsilon^{-1}$, where $\epsilon = 2r/L \ll 1$ with $2r$ being the typical filament width [12]. Optimizing swimming speed for prescribed rotation velocity, we find that swimming speed is maximized at the pitch angle $\Theta = \frac{1}{2} \arccos\left(\frac{\chi-1}{\chi+1}\right)$. For $\chi = 2$ this gives $\theta = \frac{1}{2} \arccos\left(\frac{1}{3}\right) = 35.26^\circ$ and the optimal speed is $U/\Omega R = 0.354$.

To account for a *finite width* of the filament, it was previously demonstrated [9] that one can use the slender body theory result for a prolate spheroid [10], i.e., $\chi = 2 \left(\frac{1-E/2}{1+E/2} \right) + \mathcal{O}(\epsilon^2 \ln \epsilon)$. The solid line in Fig. 5 in the main text corresponds to the RFT result in Eq. S26 with χ corrected for the finite width of the filament.

The numerical procedure used to produce results shown in Fig. 5 is based on multipole expansion scheme [11]. The filament is constructed from nearly touching N rigid spheres (“shish-kebab” filament) having the same radius r . The no-slip condition at the surface of all spheres is enforced rigorously via the use of direct transformation between solid spherical harmonics centered at origins of different spheres. The method yields a system of $\mathcal{O}(N\mathcal{L}^2)$ linear equations for the expansion coefficients and the accuracy of calculations is controlled by the number of spherical harmonics (i.e. truncation level), \mathcal{L} , retained in the series. This approach has been used before for modeling low-Reynolds-number swimmers, e.g., self-propulsion of a rotating helix through heterogenous viscous environment [9].

The spheres composing the helical filament are partitioned along the backbone of the filament $\mathbf{X}(s)$ (see Eq. (S15) and Figs. S1) so that the distance between centers of neighboring spheres is set to $2.02r$. The motion of the i th sphere composing a rotating helix can be decomposed into translation and rotation about its center as $\mathbf{V}_i = \mathbf{U}_i + \Omega \mathbf{e}_3 \times \mathbf{X}_i$ with

$\mathbf{U}_i = U\mathbf{e}_3 + \Omega\mathbf{e}_3 \times \mathbf{R}_i$; here \mathbf{R}_i is a position vector to the i th sphere center in the fixed laboratory frame and \mathbf{X}_i is the radius vector with origin at the center of i th sphere. The propulsion velocity is determined by setting the net force exerted on the rotating helix in the direction of propulsion to zero, $\sum_i F_{i3} = 0$. The normal helix shown in Fig. S1 B is

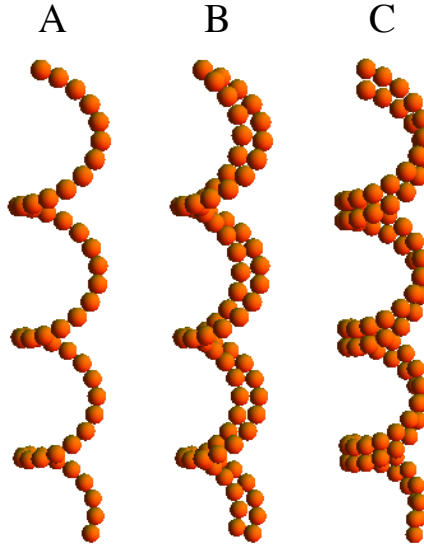


FIG. S1. Illustration of particle-based “shish-kebab” helices with $R/r = 4$, $\Theta = 57.3^\circ$ and 3.5 turns: (A) regular helix, (B) normal helix ; (C) binormal helix. The aspect ratio of the cross-section of normal and binormal helices is 2:1.

produced by positioning a helix of a smaller radius $\hat{R} = R - 2r$ *inside* a regular helix of radius R (in Fig. S1 A). The inner helix has the same pitch P as the outer helix, and thus a smaller helical angle $\hat{\Theta} = \tan^{-1}(2\pi\hat{R}/P)$. Binormal helix depicted in Fig. S1 C is obtained by stacking two identical helices of radius R one on top of the other. Normal and binormal helices of cross-sectional aspect ratio larger than 1:2 can be built from combining together three or more helices.

VII. Remanent magnetizing of helices

When the helix is placed in a strong enough magnetic field $H \gg H_a$, the magnetization \mathbf{M} of each domain saturates, e.g., orients along \mathbf{H} . In the body-fixed coordinate system $\mathbf{H} = (H \sin \alpha, 0, H \cos \alpha)$, i.e., the external field forms an angle α with the axis of helix. After removal of the field, \mathbf{M} returns to the easy axis \mathbf{e} to form the *smallest angle* between

\mathbf{M} with the previously applied field [8]. In other words, the local value of the remanent magnetization \mathbf{M}_{rem} is

$$\mathbf{M}_{rem} = M_s \operatorname{sgn}(\mathbf{H} \cdot \mathbf{e}) \mathbf{e}, \quad (\text{S27})$$

where M_s is the saturation magnetization of magnetics and $\operatorname{sgn}(x)$ is the sign function. The magnetic moment of helix is obtained from Eq. (S27) by integration over the value v of magnetic layer

$$\mathcal{M} = \int \mathbf{M}_{rem} dv = \frac{v}{L} \int_0^L \mathbf{M}_{rem} ds, \quad (\text{S28})$$

where L is the length of the filament. Here we also assume that the magnetic layer covering the helix has a constant thickness along the filament.

To determine the longitudinal (along x_3 -axis) component $\mathcal{M}_{\parallel} \equiv \mu$ and the transverse components $\mathcal{M}_{\perp} \equiv \mathbf{m}$ components of the remanent magnetizing, we need some additional assumptions about the distribution of the easy axis $\mathbf{e}(s)$. Here we consider two simplest orientations of vector $\mathbf{e}(s)$: (i) the easy axis is tangent to the centreline of helix, $\mathbf{e}(s) = \mathbf{d}_3$; (ii) the easy axis is directed along the longer cross-sectional axis of the helix, $\mathbf{e}(s) = \mathbf{d}_2$.

The calculations are performed according to Eqs. (S27) and (S28) with vectors \mathbf{d}_2 and \mathbf{d}_3 taken from Eqs. (S21) and (S22).

-
- [1] J. Gray, G. J. Hancock, *J. Exp. Biol.* 1955, **32**, 802–814.
 - [2] L. D. Landau, E. M. Lifshitz, *Mechanics*, 3rd ed.; Pergamon Press, Oxford, 1976.
 - [3] J. Diebel, *Representing Attitude: Euler Angles, Unit Quaternions, and Rotation Vectors*; Matrix, Citeseer, 2006.
 - [4] G. B. Jeffrey, *Proc. R. Soc. London A* 1922, **102**, 161–179.
 - [5] L. D. Landau, E. M. Lifshitz, *Electrodynamics of Continuous Media*, 2nd ed.; Pergamon Press, Oxford, 1984.
 - [6] A. Ghosh, D. Paria, H. J. Singh, P. L. Venugopalan, A. Ghosh, *Phys. Rev. E* 2012, **86**, 031401.
 - [7] A. F. da Fonseca, C. P. Malta, D. S. Galvao, *Nanotechnology* 2006, **17**, 5620–5626.
 - [8] S. Shtrikman, D. Treves, *J. Appl. Phys.* 1960, **31**, 58S–66S.
 - [9] A. M. Leshansky, *Phys. Rev. E* 2009, **80**, 051911.
 - [10] J. P. K. Tillett, *J. Fluid Mech.* 1970, **44**, 401–417.

- [11] A. V. Filippov, *J. Colloid Interface Sci.* 2000, **229**, 184–195.
- [12] S. Kim, S. J. Karrila, *Microhydrodynamics*; Butterworth–Heinemann, Boston, 1991.